

# (25143) Itokawa: The Power of Radiometric Techniques for the Interpretation of Remote Thermal Observations in the Light of the Hayabusa Rendezvous Results\*

Thomas G. MÜLLER

*Max-Planck-Institut für extraterrestrische Physik, Giessenbachstraße, 85748 Garching, Germany*  
*tmueller@mpe.mpg.de*

Sunao HASEGAWA

*Institute of Space and Astronautical Science, Japan Aerospace Exploration Agency, 3-1-1 Yoshinodai,  
Chuo-ku, Sagamihara 252-5210*  
*hasehase@isas.jaxa.jp*

and

Fumihiko USUI

*Department of Astronomy, Graduate School of Science, The University of Tokyo, 7-3-1 Hongo,  
Bunkyo-ku, Tokyo 113-0033*  
*usui@astron.s.u-tokyo.ac.jp*

(Received ; accepted )

## Abstract

The near-Earth asteroid (25143) Itokawa was characterised in great detail by the Japanese Hayabusa mission. We revisited the available thermal observations in the light of the true asteroid properties with the goal to evaluate the possibilities and limitations of thermal model techniques. In total, we used 25 published ground-based mid-infrared photometric observations and 5 so far unpublished measurements from the Japanese infrared astronomical satellite AKARI in combination with improved H-G values (absolute magnitude and slope parameter). Our thermophysical model (TPM) approach allowed us to determine correctly the sense of rotation, to estimate the thermal inertia and to derive robust effective size and albedo values by only using a simple spherical shape model. A more complex shape model, derived from light-curve inversion techniques, improved the quality of the predictions considerably and made the interpretation of thermal light-curve possible. The radiometrically derived effective diameter value agrees within 2% of the true Itokawa size value. The combination of our TPM and the final (25143) Itokawa in-situ shape model was then used as a benchmark for deriving and testing radiometric solutions. The consolidated value for the surface-averaged thermal inertia is  $\Gamma = 700 \pm 200 \text{ J m}^{-2} \text{ s}^{-0.5} \text{ K}^{-1}$ . We found

that even the high resolution shape models still require additional small-scale roughness in order to explain the disk-integrated infrared measurements. Our description of the thermal effects as a function of wavelengths, phase angle, and rotational phase facilitates the planning of crucial thermal observations for sophisticated characterization of small bodies, including other potentially hazardous asteroids. Our analysis shows the power of radiometric techniques to derive the size, albedo, thermal inertia, and also spin-axis orientation from small sets of measurements at thermal infrared wavelengths.

**Key words:** infrared: solar system — minor planets, asteroids: individual: (25143) Itokawa — radiation mechanisms: thermal — techniques: photometric

## 1. Introduction

The Near-Earth asteroid (NEA) (25143) Itokawa (1998 SF36) is one of the best studied asteroids in our Solar System. It was the sample return target of the Japanese Hayabusa (MUSES-C) mission. The spacecraft was in close proximity to the asteroid from September through early December 2005. As a result of the encounter, the asteroid has been characterised in great detail: (25143) Itokawa is an irregularly formed body consisting of a loose pile of rubble rather than a solid monolithic asteroid (Fujiwara et al. 2006; Saito et al. 2006; Abe et al. 2006b). Its appearance is boomerang-shaped and composed of two distinct parts with faceted regions and a concave ring structure in-between (Demura et al. 2006). Recently, the detection of YORP spin-up revealed that the two distinct parts of Itokawa have different densities and are likely to be two merged asteroids (Lowry et al. 2014). Its effective diameter (of an equal volume sphere) is  $327.5 \pm 5.5$  m (volume of  $(1.840 \pm 0.092) \times 10^7$  m<sup>3</sup>; Fujiwara et al. 2006). This compares very well with the pre-encounter size prediction obtained via radiometric techniques by Müller et al. (2005) (M05 hereafter) of  $D_{\text{eff}} = 320 \pm 30$  m. The radar size prediction is about 16% too high (Ostro et al. 2004; Ostro et al. 2005). The mass is estimated as  $(3.58 \pm 0.18) \times 10^{10}$  kg, implying a bulk density of  $(1.95 \pm 0.14)$  g cm<sup>-3</sup> (Abe et al. 2006b). The retrograde pole orientation in ecliptic coordinates is  $(\lambda_{\text{pole}}, \beta_{\text{pole}}) = (128.5^\circ, -89.66^\circ)$ , with a 3.9° margin of error (Demura et al. 2006). Itokawa is classified as an SIV-type asteroid via ground-based near-infrared (NIR) spectroscopy (Binzel et al. 2001), a type common in the inner portion of the asteroid belt. These measurements at mineralogically diagnostic wavelength show similarities to ordinary chondrites and/or primitive achondrite meteorites. Hayabusa confirmed the S-class asteroid characteristics and revealed an olivine rich mineral assemblage of the surface, similar to LL5 or LL6 chondrites (Abe et al. 2006a; Okada et al. 2006). The most recent geometric albedo estimate of  $p_V = 0.29 \pm 0.02$  comes from ground-based visual photometry combined with Hayabusa-derived size

---

\* Based on observations with AKARI, a JAXA project with the participation of ESA.

information (Bernardi et al. 2009). The surface is dominated by regions with brecciated rocks and regions with a coarse-grain-filled surface with thermal inertias between that of monolithic rocks ( $\Gamma \sim 4000 \text{ J m}^{-2} \text{ s}^{-0.5} \text{ K}^{-1}$ ) and powdery surface like lunar regolith ( $\Gamma \sim 40 \text{ J m}^{-2} \text{ s}^{-0.5} \text{ K}^{-1}$ ) (Yano et al. 2006; Noguchi et al. 2010). M05 used a sample of remote, disk-integrated thermal measurements to derive the average thermal inertia of Itokawa’s top surface layer. They found a thermal inertia value of roughly  $750 \text{ J m}^{-2} \text{ s}^{-0.5} \text{ K}^{-1}$ . A study by Mueller (2007) found a very similar value of  $700 \text{ J m}^{-2} \text{ s}^{-0.5} \text{ K}^{-1}$ . Gundlach & Blum (2013) combined the thermal inertia value with Itokawa’s known size and low gravitational acceleration on the surface to determine a mean surface particle radius of  $21_{-14}^{+3} \text{ mm}$  which is in nice agreement with in-situ observations presented by Yano et al. (2006) and Kitazato et al. (2008). One aspect of our work here was to test the derived (pre-Hayabusa) thermal properties (mainly the object’s thermal inertia) in the light of the in-situ results.

We re-visit the available remote, disk-integrated thermal data, comprising ground-based observations in standard N- and Q-band filters with IRTF/MIRSI and ESO/TIMMI2, and from AKARI, the Japanese infrared astronomical satellite (Murakami et al. 2007). The goal of our study is to describe the possibilities and limitations of radiometric methods when using remote, disk-integrated data, as available or easily obtainable for most of the minor bodies. The derived values are then directly compared to the in-situ results from the Hayabusa-mission. By comparing the results from the radiometric techniques with the in-situ results, we validate model techniques and provide observing strategies for future applications to other targets, including potentially hazardous asteroids (PHAs).

Section 2 gives an overview of the existing thermal observations and describes the so far unpublished observations by AKARI. In Section 3 we describe the different TPM applications and optimisation processes which we applied to the full dataset of remote thermal observations and present the derived results: Section 3.1 describes briefly the thermophysical model (TPM) and the range of possible input parameters. In a first analysis step we use a spherical shape model with a range of pro- and retrograde spin-vectors (Section 3.2). In the second step (Section 3.3) we added the shape and spin-vector information derived from light-curve inversion techniques. In the third step (Section 3.4) we used the true shape model and spin-vector solution as provided by the Hayabusa mission. The flux predictions from the best TPM solution are then compared with the available observations. In Section 4 we inter-compare different shape solutions with respect to thermal light-curves and predict the behaviour of the spectral energy distribution (SED), the thermal light-curve amplitude, shape, and the thermal beaming effect. In Section 5 we discuss the potential and the limitation of the radiometric methods, using the various levels of information. The summary and transfer of applications to other targets is given in Section 6.

**Table 1.** Summary of mid-IR observing sets for asteroid (25143) Itokawa.

No*	Time <sup>†</sup> [UT]	Filter Band	$r^{\ddagger}$ [AU]	$\Delta^{\S}$ [AU]	$\alpha^{\parallel}$ [ $^{\circ}$ ]	Remarks
21	2004/Jul/10 11:45	N11.7	1.060399	0.049983	+28.32	IRTF/MIRSI (Mueller M. et al. in press) <sup>#</sup>
22	2004/Jul/10 11:48	N11.7	1.060407	0.049990	+28.31	IRTF/MIRSI (Mueller M. et al. in press) <sup>#</sup>
23	2004/Jul/10 13:32	N11.7	1.060673	0.050243	+28.18	IRTF/MIRSI (Mueller M. et al. in press) <sup>#</sup>
24	2004/Jul/10 13:41	N9.8	1.060696	0.050266	+28.17	IRTF/MIRSI (Mueller M. et al. in press) <sup>#</sup>
25	2004/Jul/10 13:51	N9.8	1.060721	0.050290	+28.16	IRTF/MIRSI (Mueller M. et al. in press) <sup>#</sup>
26	2007/Jul/26 11:29	N4	1.053777	0.281244	-73.49	AKARI (this work)**
27	2007/Jul/26 11:29	S7	1.053777	0.281244	-73.49	AKARI (this work)**
28	2007/Jul/26 11:28	S11	1.053774	0.281244	-73.49	AKARI (this work)**
29	2007/Jul/26 13:09	L18	1.054027	0.281282	-73.43	AKARI (this work)**
30	2007/Jul/26 13:12	L24	1.054035	0.281283	-73.43	AKARI (this work)**

Notes. \*Observations with running numbers 1-20 are listed in table 1 in M05. <sup>†</sup>The times are mid observing times in the observer's time frame. <sup>‡</sup>The heliocentric distance. <sup>§</sup>The observer-centric distance. <sup>||</sup>The phase angles, negative before opposition and positive after. <sup>#</sup>The observations in Mueller M. et al. (in press) have been shifted to the observer's time frame by adding 25 s to the light-time corrected times given in the publication. \*\*The geometry is given by the geocentric calculation.

## 2. Thermal Observations and Input Data

We combine five previously published mid-infrared observations by Mueller M. et al. (in press) with 20 observations by M05 and five dedicated AKARI observations. The M05 data (table 1 & 3 in M05) have running indices from 1 to 20. The additional data presented here are labeled 21-25 and 26-30 respectively (table 1 and table 2).

### 2.1. IRTF/MIRSI observations

Mueller M. et al. (in press) presented a set of five N-band observations which we included in our calculations. For the entries in table 1 and table 2 (numbers 21-25) we used the monochromatic, colour-corrected fluxes (but now in Jansky-units) and calculated the true observing times (Mueller M. et al. in press gave times which were corrected for 1-way light-time, i.e., in the asteroid time frame). Mueller (2007) mentioned that they had taken the observations at a relatively high level of atmospheric humidity. In addition, all observations were taken at air-masses larger than 2 due to technical problems at meridian transit.

### 2.2. AKARI observations

Asteroid (25143) Itokawa was observed on July 27, 2007 by the NIR, MIR-S, and MIR-L channels on the infrared camera IRC (Onaka et al. 2007) on-board AKARI. During one

pointed observation, all three IRC channels obtained images simultaneously, covering different wavelength ranges. The NIR and MIR-S channels share the same field of view, while the MIR-L channel observes a region which is  $\sim 20'$  away from the field centre of the NIR and MIR-S channels. In total, two pointed observations on Itokawa were carried out to obtain data in all three channels. The Astronomical Observation Template (AOT) IRC02 for dual-filter photometry (see Onaka et al. 2007 for details) was used. As a result, observations for Itokawa with the NIR, MIR-S, and MIR-L were performed in the filters N3 (reference wavelength of  $3.2 \mu\text{m}$ , but not used here for our thermal analysis), N4 ( $4.1 \mu\text{m}$ ), S7 ( $7.0 \mu\text{m}$ ), S11 ( $11.0 \mu\text{m}$ ), L15 ( $15.0 \mu\text{m}$ ) and L24 ( $24.0 \mu\text{m}$ ) with effective bandwidths of 0.9, 1.5, 1.8, 4.1, 6.0 and  $5.3 \mu\text{m}$ , respectively. The projected area of the NIR channels was about  $10.0' \times 9.5'$  which corresponds to an angular resolution of  $1.5''/\text{pixel}$ . The MIR-S channels of the IRC have pixel sizes of about  $2.3''/\text{pixel}$ , giving a field of view about  $10.0' \times 9.1'$ . The MIR-L channel was used with a image scale of  $2.4''/\text{pixel}$ , giving a  $10.2' \times 10.3'$  sky field. For the data processing the IRC imaging data pipeline<sup>1</sup> was used. The AKARI telescope was not able to track moving objects such as comets and asteroids. Therefore, a centroid determination in combination with a standard shift-and-add technique was performed, followed by median processing to obtain better photometric accuracy. Aperture photometry on IRC images was carried out using the APPHOT task of IRAF through circular aperture radii of 10.0 (in the NIR channel) and 7.5 (in the MIR-S and MIR-L channels) pixels, which are also used for the standard star flux calibration. The resulting astronomical data units were converted to the calibrated flux densities by using the IRC flux calibration constants in the *Revisions of the IRC conversion factors*<sup>2</sup>. Colour differences between calibration stars and Itokawa were not negligible due to the wide bandwidths of the IRC. Colour correction factors were obtained using both predicted thermal flux of Itokawa and the relative spectral response functions for IRC. Colour correction fluxes of Itokawa were obtained by dividing the quoted fluxes by 1.453 in N4 band, 1.020 in S7 band, 0.956 in S11 band, 0.960 in L18 band, and 1.079 in L24 band. The observational results are summarised in table 2 (numbers 26-30) and further details about AKARI asteroid observations and catalogued data are given in Usui et al. (2011); Hasegawa et al. (2013).

### 3. Thermophysical Modelling

#### 3.1. Description of the Thermophysical Model

We applied the radiometric technique as described in M05. Via a  $\chi^2$ -process, with diameter and thermal inertia as free parameters<sup>3</sup>, we searched for the best solution to match

<sup>1</sup> AKARI IRC Data Users Manual ver.1.3, <http://www.ir.isas.jaxa.jp/ASTRO-F/Observation/>

<sup>2</sup> [http://www.ir.isas.jaxa.jp/ASTRO-F/Observation/DataReduction/IRC/ConversionFactor\\_071220.html](http://www.ir.isas.jaxa.jp/ASTRO-F/Observation/DataReduction/IRC/ConversionFactor_071220.html)

<sup>3</sup> We also solve for the geometric albedo, but is not considered as a free parameter since it is tightly connected to the H-magnitude via the size information:  $p_V = 10^{(2 \cdot \log_{10}(S_0) - 2 \cdot \log_{10}(D_{eff}) - 0.4 \cdot H_V)}$ , with the Solar constant

**Table 2.** Summary of the available thermal infrared observations of asteroid (25143) Itokawa.

No*	Filter	$\lambda_c$ [ $\mu\text{m}$ ]	FD [Jy]	$\sigma_{\text{err}}$ [Jy]	Remarks
21	N11.7	11.7	0.762	0.100	IRTF/MIRSI (Mueller M. et al. in press) <sup>†</sup>
22	N11.7	11.7	0.721	0.091	IRTF/MIRSI (Mueller M. et al. in press) <sup>†</sup>
23	N11.7	11.7	0.913	0.114	IRTF/MIRSI (Mueller M. et al. in press) <sup>†</sup>
24	N9.8	9.8	0.791	0.125	IRTF/MIRSI (Mueller M. et al. in press) <sup>†</sup>
25	N9.8	9.8	0.570	0.122	IRTF/MIRSI (Mueller M. et al. in press) <sup>†</sup>
26	N4	4.1	0.00032	0.00025	AKARI (this work)
27	S7	7.0	0.00469	0.00028	AKARI (this work)
28	S11	11.0	0.01422	0.00053	AKARI (this work)
29	L15	15.0	0.02137	0.00079	AKARI (this work)
30	L24	24.0	0.01947	0.00120	AKARI (this work)

Notes. \*Observations with running numbers 1-20 are listed in table 1 in M05. <sup>†</sup>The flux densities in Mueller M. et al. (in press) have been converted to Jansky.

all thermal observations listed in Sect. 2 simultaneously:  $\chi^2 = 1/(N - \nu)\Sigma((obs - mod)^2)$ , with  $\nu$  being the number of free parameters (here  $\nu=2$ , with size and thermal inertia as free parameters). The detailed steps are described in Müller et al. (2011). The TPM is detailed by Lagerros (1996); Lagerros (1997); Lagerros (1998a); Lagerros (1998b); Harris & Lagerros (2002). It places the asteroid at the true illumination and observing geometry. For each surface element the solar insolation is taken into account and the amount of reflected light and thermal emission are calculated, controlled by the albedo, the H-G values, the surface roughness (parameterised by  $\rho$ , the r.m.s. of the surface slopes and  $f$ , the fraction of the surface covered by craters) and the thermal inertia  $\Gamma$ . For the temperature calculation the one-dimensional vertical heat conduction (controlled by the thermal inertia<sup>4</sup>  $\Gamma$ ) into the surface is taken into account. The treatment of heat conduction inside the spherical section craters is approximated by using the brightness temperature relations as a function of the thermal parameter<sup>5</sup>  $\Theta$  for a flat surface (Lagerros 1998a). In this way it is possible to separate the beaming from the heat conduction which is relevant for computation speed reasons. A summary of the influences of the thermal parameters as a function of wavelength and as a function of phase angle is given in Müller (2002). The technique to determine thermal properties from a set of thermal observations was

---


$$S_0 = 1366 \text{ W m}^{-2}.$$

<sup>4</sup> The thermal inertia  $\Gamma$  is defined as  $\sqrt{\kappa\rho c}$ , where  $\kappa$  is the thermal conductivity,  $\rho$  is the density, and  $c$  is the heat capacity.

<sup>5</sup> The thermal parameter  $\Theta$  is defined as  $(\Gamma \sqrt{\omega}) / (\epsilon\sigma T_{ss}^3)$ , where  $\Gamma$  is the thermal inertia,  $\omega$  is the angular velocity of rotation and  $T_{ss}$  is the sub-solar temperature.

**Table 3.** Summary of general TPM input parameters and applied variations.

	Range	Units/Remarks	M05 value
$\Gamma$	0...2500	[J m <sup>-2</sup> s <sup>-0.5</sup> K <sup>-1</sup> ] thermal inertia	750
$\rho$	0.1...0.9	rms. of surface slopes	0.7
$f$	0.4...0.9	fraction of surface covered by craters	0.6
$\epsilon$	0.9	$\lambda$ -independent emissivity	0.9
$H_V$	19.40 <sup>+0.10</sup> <sub>-0.09</sub>	[mag] Bernardi et al. (2009)	19.9
$G$	0.21 <sup>+0.07</sup> <sub>-0.06</sub>	Bernardi et al. (2009)	0.21
$P_{\text{sid}}$	12.13237 $\pm 0.00008$	[h] Kaasalainen et al. (2003, in press)	12.13237

already successfully applied for large main-belt asteroids by e.g., Spencer et al. (1989); Müller & Lagerros (1998); Müller & Lagerros (2002); Müller et al. (1999); O’Rourke et al. (2012) and a range of near-Earth asteroids (e.g., Müller et al. 2011; Müller et al. 2012; Müller et al. 2013).

The general TPM input parameters and parameter ranges are listed in table 3. The first three parameters show the physically meaningful range for thermal properties (see e.g., Lagerros 1998b). The constant emissivity is a standard value used in radiometric techniques when applied to mid-infrared data (e.g., Lebofsky et al. 1986). The last three values are derived from visual photometric measurements.

### 3.2. Using a spherical shape model

The shapes and spin-axis orientations are not known for most of the asteroids. It is therefore very instructive to start the radiometric technique with the simplest shape model to evaluate the possibilities and limitations of such a simple approach. In a first attempt to interpret the thermal observations we use a spherical shape model with a range of pro- and retrograde spin-vector orientations ( $\beta_{\text{ecl}}^{SV} = \pm 30/60/90^\circ$ , arbitrary  $\lambda_{\text{ecl}}^{SV}$ ) and the values specified in table 3. Figure 1 shows the implementation of this model for the observation Nr. 12 (table 1 in M05) at a phase angle of  $54^\circ$  (01-Jul-2004 06:03 UT) for a  $+90^\circ$  prograde (top) and  $-90^\circ$  retrograde (bottom) sense of rotation. The temperature pictures, as seen from the observer, are very different and consequently also the connected disk-integrated thermal fluxes. The illustration shows that the combination of thermal observations from before and after opposition (with either warm or cold terminator) can indicate the true sense of rotation.

The  $\chi^2$ -figure (figure 2) shows that the best agreement between observations and model

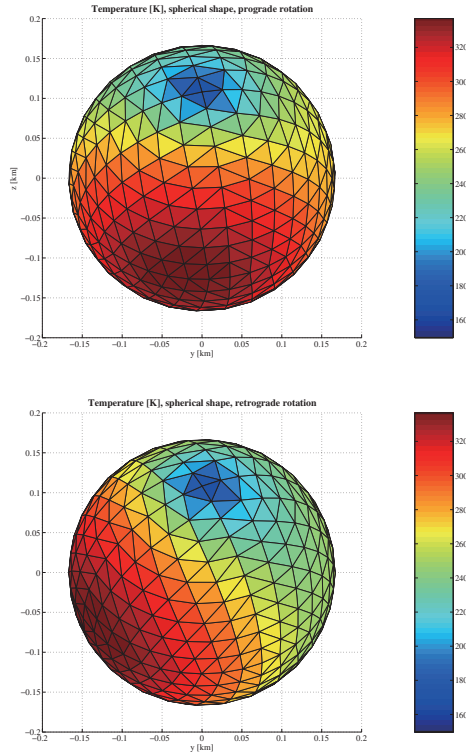


**Fig. 1.** The pro- and retrograde implementation of the spherical shape model for the epoch 01-Jul-2004 06:03 UT. For the temperature calculation a thermal inertia of  $700 \text{ J m}^{-2} \text{ s}^{-0.5} \text{ K}^{-1}$  has been used. The viewing geometry is in the ecliptic coordinate system (spin vector perpendicular to the ecliptic plane) as seen from Earth, projected on the sky. The Sun is at a phase angle of  $54^\circ$ . The asteroid's apparent position (Earth-centred) was  $312^\circ$  ecliptic longitude and  $-48^\circ$  ecliptic latitude.

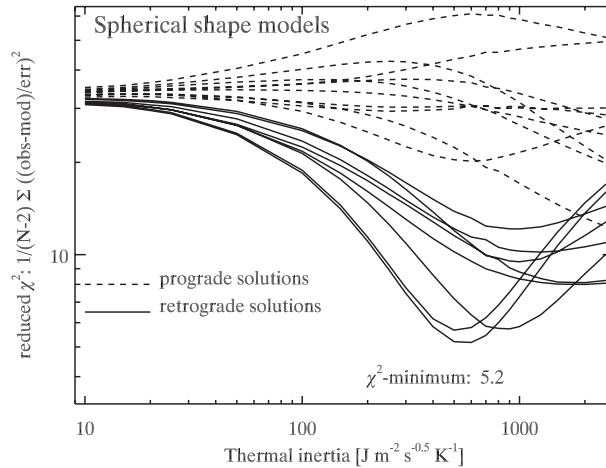


**Fig. 2.** The thermal inertia  $\chi^2$  optimisation process for all thermal observations, assuming a spherical shape model and 18 different pro- and retrograde spin-axes orientations (at latitudes  $\pm 30^\circ$ ,  $\pm 60^\circ$ ,  $\pm 90^\circ$ , and arbitrary longitudes).



predictions are found for models with a retrograde sense of rotation. The prograde rotation options have much higher  $\chi^2$ -values and often show no clear minimum within the very large range of thermal inertias. In addition to clear indications for the sense of rotation the  $\chi^2$ -analysis also points towards thermal inertias in the approximate range  $400\text{-}1200 \text{ J m}^{-2} \text{ s}^{-0.5} \text{ K}^{-1}$  where the lowest  $\chi^2$ -values are found. The 3 curves with lowest  $\chi^2$ -minima are connected to  $(\lambda_{ecl}^{SV}, \beta_{ecl}^{SV}) = (90^\circ, -60^\circ), (60^\circ, -30^\circ), (0^\circ, -90^\circ)$ . On basis of our photometric data set and without using additional visual light-curve information, it is apparently not possible to constrain the spin-axis orientation further within the retrograde domain.

The connected effective radiometric diameter ( $\beta_{ecl}^{SV} = -90^\circ$ ) is  $0.31 \pm 0.04 \text{ km}$ , the geometric albedo  $0.30 \pm 0.06$  (mean and r.m.s. of the radiometric solution for the 30 individual observations). The diameter/albedo values for the low  $\chi^2$ -minima connected to the pole-solutions  $(90^\circ, -60^\circ)$  and  $(60^\circ, -30^\circ)$  are within this error range.

### 3.3. Using a shape model from light-curve inversion technique

Kaasalainen et al. (in press) published a shape model with a spin-vector solution based on a large set of remote, disk-integrated photometric light-curve observations during the years 2000 to 2004. The long time-line allowed to determine an accurate rotation period, a high quality pole solution, and a shape estimate. The shapes derived from light-curve inversion techniques are reproducing the existing set of visual light-curves, but they do not have an absolute size information connected to it. The Kaasalainen shape model for (25143) Itokawa has 1022 vertices and 2040 facets and it agreed well with the radar-based solution (Ostro et al. 2005).

The rotation parameters are  $\beta_{pole} = -89^\circ \pm 5^\circ$  (retrograde sense of rotation),  $\lambda_{pole} = 330^\circ$  for the ecliptic latitude and longitude of the pole, and  $P = 12.13237 \pm 0.00008 \text{ h}$  for the sidereal period. The zero rotational phase ( $\gamma_0 = 0.0^\circ$ ) of this shape model is connected to a zero time of  $T_0 = 2451933.95456$ . Our TPM implementation of this Kaasalainen shape model was tested and verified on absolute times and rotational phases against the highest quality visual light-curves. Figure 3 (top) shows the temperature-coded (based on our best TPM parameters) shape model as seen from the observer on 01-Jul-2004 06:03 UT (observational data point number 12 in table 1 in M05).

We repeated the  $\chi^2$ -procedure (see M05 and Sect. 3.2) with the given Kaasalainen spin-vector for a range of thermal inertias. The primary goal was to determine the effective size of the scale-free Kaasalainen shape-model and to narrow down the possible thermal inertia of Itokawa's surface. This time we also modified the TPM surface roughness to investigate the influence in the optimisation process (figure 4). The new minimum of 2.9 in the  $\chi^2$ -calculations (lowest solid line in figure 4) is now significantly lower than in the case of a spherical shape model, indicating that the effects of the non-spherical shape are clearly dominating the  $\chi^2$ -optimisation. But the  $\chi^2$ -values are still relatively high and show that some data points are not

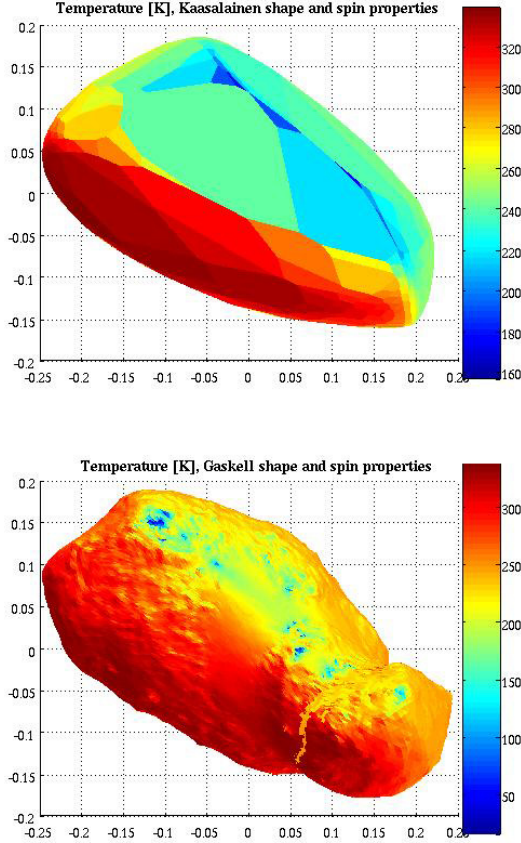


**Fig. 3.** The implementation of the Kaasalainen shape model with 2040 facets (top) and the Gaskell shape model with 49 152 facets (bottom) for the epoch 01-Jul-2004 06:03 UT. For the temperature calculation a thermal inertia of  $700 \text{ J m}^{-2} \text{ s}^{-0.5} \text{ K}^{-1}$  has been used. The viewing geometry is in the ecliptic coordinate system as seen from Earth, projected on the sky. The Sun is at a phase angle of  $54^\circ$ . The asteroid's apparent position (Earth-centred) was  $312^\circ$  ecliptic longitude and  $-48^\circ$  ecliptic latitude.

well matched. In a second round of  $\chi^2$ -calculations we deselected all data which are marked as taken under bad weather conditions (labeled with  $\star$  in M05 and airmass  $> 2.0$  data by Mueller M. et al. in press). The results are shown as dashed lines in figure 4. Now, the reduced- $\chi^2$  minimum is at 0.9 and we obtained an excellent match between observed fluxes and model predictions. Our findings can be summarised as follows: (1) Additional surface roughness is needed in the modelling to obtain acceptable  $\chi^2$ -solutions. Without roughness (dotted lines in figure 4) the  $\chi^2$ -minima are a factor 2-3 higher, mainly caused by the poor match to the data at shortest wavelengths and smallest phase angles. (2) The surface roughness influences the calculations. It plays an important role at mid-IR wavelength where the thermal infrared emission peaks (see also Müller 2002): roughness variations cause a change in SED slopes and in second order also a change in absolute thermal fluxes, with different impact at different phase angles. Depending on the surface roughness, the minima in figure 4 are shifting slightly and

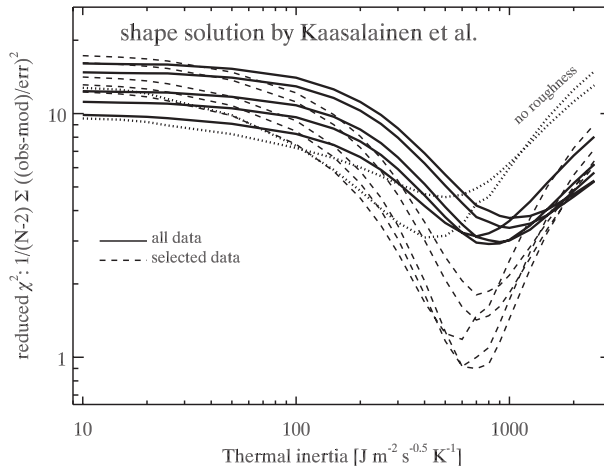


**Fig. 4.** The thermal inertia  $\chi^2$ -optimisation process for all thermal observations (solid lines) and a selected subset (dashed lines) assuming the shape model from Kaasalainen et al. (in press). The two dotted lines represent the corresponding results for a smooth surface without additional roughness. The 5 solid lines and the 5 dashed lines are the results for different levels of roughness ranging from a relatively smooth surface ( $\rho=0.4$ ,  $f=0.4$ ) to an extremely rough surface completely covered by hemispherical craters ( $\rho=1.0$ ,  $f=1.0$ ).

therefore add to the thermal inertia uncertainty. (3) At a certain level of surface roughness it is not possible anymore to distinguish between roughness influence and thermal inertia influence. More observational data closer to opposition would be needed to disentangle these competing surface properties in the TPM. (4) The full dataset and also the selected high-quality dataset show the  $\chi^2$ -minima at similar thermal inertias: The most likely thermal inertia solutions are in the range  $600\text{--}1100 \text{ J m}^{-2} \text{ s}^{-0.5} \text{ K}^{-1}$  (higher values are connected to higher levels of surface roughness and vice versa). (5) The quality limitations of our set of thermal observations determine the  $\chi^2$ -minima. A few low quality photometric observations dominate the final uncertainties. (6) The corresponding effective radiometric diameter is  $0.320 \pm 0.029 \text{ km}$ , the geometric albedo  $0.299 \pm 0.043$  at a thermal inertia of  $800 \text{ J m}^{-2} \text{ s}^{-0.5} \text{ K}^{-1}$ . These values are in excellent agreement with the in-situ results.

#### 3.4. Using the in-situ shape model

One result from the Hayabusa-mission is the highly accurate physical description of (25143) Itokawa. These shape models were produced by Robert Gaskell and available in different resolutions from <http://sbn.psi.edu/pds/resource/itokawashape.html>. The four resolutions correspond to  $6(Q+1)^2$  vertices and  $12Q^2$  facets, with  $Q = 64, 128, 256, 512$ . The models include many small-scale features on the surface seen by the Hayabusa-mission during close flybys. The Gaskell shape model is scaled to the true object size which corresponds to an effective diameter  $D_{\text{eff}} = 0.334 \text{ km}$  of an equal volume sphere.

**Table 4.** Summary of the critical radiometrical properties from different sources. The numbers in bold face indicate the current best values.

Source	Size/Shape $D_{eff}$ [m]	colours & geom. albedo $p_V$	thermal params $\eta$ or $\Gamma$ [ $\text{Jm}^{-2}\text{s}^{-0.5}\text{K}^{-1}$ ]	Remarks/ Comments
Ostro et al. 2001	630( $\pm 60$ ) $\times$ 250( $\pm 30$ ) m	—	—	radar 2001
Sekiguchi et al. 2003	352 $^{+28}_{-32}$ m	0.23 $^{+0.07}_{-0.05}$	NEATM <sup>1</sup> - $\eta = 1.2$	single N-band
Ohba et al. 2003	a/b=2.1, b/c=1.7; triaxial ellipsoid	—	—	light-curve inversion
Isighuro et al. 2003	620( $\pm 140$ ) $\times$ 280( $\pm 60$ ) $\times$ 160( $\pm 30$ ) m	0.35 $\pm 0.11$	FBM <sup>2</sup> - $\eta = 1.1$	M' & N-band
Kaasalainen et al. 2003	a/b=2.0, b/c=1.3; triaxial shape	no variegation	—	light-curve inversion
Ostro et al. 2004	548 $\times$ 312 $\times$ 276 m; 358 ( $\pm 10\%$ ) m	no variegation	—	radar 2001
Ostro et al. 2005	594 $\times$ 320 $\times$ 288 m; 364 ( $\pm 10\%$ ) m	—	—	radar 2001-2004
Kaasalainen et al. in press	improved triaxial shape	—	—	light-curve inversion
Mueller M. et al. in press	$D_{eff}=280$ m	—	$\Gamma=350$	multi-epoch M'/N-data
Müller et al. 2005	$D_{eff}=320\pm 30$ m	0.19 $^{+0.11}_{-0.03}$	$\Gamma=750\pm 250$	multi-epoch N-/Q-data
Lowry et al. 2005	a/b>2.14	colours; spec. slope	—	BVRI photometry
Demura et al. 2006	535 $\times$ 294 $\times$ 209( $\pm 1$ ); <b>327.5<math>\pm</math>5.5 m</b>	—	—	in-situ
Thomas-Osip et al. 2008	a/b=1.9 $\pm$ 0.1	0.23 $\pm$ 0.02; $H_V$	—	V & NIR observations
Gaskell et al. 2008	$D_{eff} = 334$ m; <b>highres. shape models</b>	—	—	Hayabusa/AMICA
Bernardi et al. 2009	—	<b><math>H_V</math> &amp; G-slope</b>	—	V-band data
this work (Sect. 3.2)	310 $\pm$ 40 m; spin-axis estimate	0.30 $\pm$ 0.06	$\Gamma= 400$ -1200	spherical shape
this work (Sect. 3.3)	320 $\pm$ 29 m	0.299 $\pm$ 0.043	$\Gamma = 600$ -1100	lc-inversion shape
this work (Sect. 3.4)	—	<b>0.29 <math>\pm</math> 0.02</b>	$\Gamma =$ <b>500-900</b>	in-situ shape

Notes. <sup>1</sup>NEATM: Near-Earth Asteroid Thermal Model; <sup>2</sup>FBM: free beaming parameter thermal model.

### 3.4.1. Determination of the geometric albedo

The true-size shape model allows now to investigate the influence of the aspect angle (defined such that it equals 0° when observing the North pole and it equals 180° when observing the South pole of the object) on H-mag calculations and consequently also on the determination of the geometric albedo (see also O'Rourke et al. 2012 on similar considerations for (21) Lutetia).

Bernardi et al. (2009) measured V-magnitudes of Itokawa for a wide range of phase angles and determined the corresponding mean light-curve values via a fit of synthetic light-curves (using the Gaskell shape model) to the observed incomplete light-curves. But depending on the aspect angle, the light-curved averaged cross-section can vary between about 320 m and 410 m! The relevant cross-sections (phase angles < 40°) for the H-mag determination in Bernardi et al. (2009) were all very small (324 $\pm$ 4 m instead of 332 m used by Bernardi et al. 2009). Their derived H-mag of 19.40 $^{+0.10}_{-0.09}$  mag is therefore only applicable for this smaller cross-section. The corresponding geometric albedo  $p_V$  (relations in Bowell et al. 1989) is 0.31 $\pm$ 0.03.

Thomas-Osip et al. (2008) published a  $H_V$  of 19.472 $\pm$ 0.006 mag based on observations taken in 2004 covering a wide phase angle range. We calculated the corresponding aspect angles

and found again that the light-curve-averaged cross-section diameters (at crucial phase angles  $< 40^\circ$ ) were slightly smaller (just around 0.330 km) than the effective diameter of the Gaskell shape model (of an equal volume sphere). The corresponding geometric albedo  $p_V$  is  $0.28 \pm 0.02$ .

These observations from 2000, 2001 and 2004 cover a huge phase angle range between 4 and  $129^\circ$  and aspect angles from 50 to about  $150^\circ$ . Merging both datasets and considering the aspect angle limitations of the individual sets, we assign a geometric albedo of  $0.29 \pm 0.02$  for our TPM calculations (based on a solar constant<sup>6</sup> of  $1366 \text{ W m}^{-2}$ ). The true, object-connected H-mag, averaged over all aspect angles and connected to the average size of an equal volume sphere, is then  $H_V = 19.4 \pm 0.1 \text{ mag}$ .

#### 3.4.2. Verification of radiometric size and thermal inertia

Similar to our analysis in Sect 3.2 and 3.3 we determined the size, albedo and thermal inertia information through our TPM implementation and using the ‘‘Gaskell’’ shape model with the absolute size as a free parameter. The corresponding  $\chi^2$ -picture is very similar to figure 4. We obtained minimum (reduced)  $\chi^2$ -values around 3 for the full data-set and just below 1 for the high-quality sub-set of observations. The best match between observations and model predictions was found for an effective size of  $0.332 \pm 0.033 \text{ km}$  and a geometric albedo of  $0.30 \pm 0.05$  (smaller errors if we only use the high-quality subset of data). These means and standard deviations are connected to a thermal inertia of  $700 \text{ J m}^{-2} \text{ s}^{-0.5} \text{ K}^{-1}$  at the  $\chi^2$ -minimum and assuming an intermediate level of surface roughness. The radiometrical size derived in this way is in excellent agreement with the true in-situ size. This validates our model implementation and analysis technique. But similar to figure 4, we see a small shift in thermal inertia when we modify the roughness level. An extremely rough surface ( $f=1.0$ ,  $\rho=1.0$ : 100% of the surface covered by hemispherical craters with a surface slope r.m.s. of 1) requires slightly higher thermal inertias up to about  $900 \text{ J m}^{-2} \text{ s}^{-0.5} \text{ K}^{-1}$ . A smoother surface ( $f=0.4$ ,  $\rho=0.4$ : 40% of the surface covered by shallow craters with a surface slope r.m.s. of 0.4) has to be combined with a lower thermal inertia ( $500 \text{ J m}^{-2} \text{ s}^{-0.5} \text{ K}^{-1}$ ) to obtain a good match between model predictions and observed fluxes. This possible range for the thermal inertia can be translated into a mean grain radius of the surface regolith of about  $21_{-14}^{+3} \text{ mm}$  (Gundlach & Blum 2013) which is in excellent agreement with the in-situ findings (Yano et al. 2006; Kitazato et al. 2008). The heat transport within the top-surface layers is therefore dominated by radiation effects and material properties play a very small role for the thermal behaviour of Itokawa.

We also tested thermal model solutions without adding any additional roughness. The  $\chi^2$ -test produced an acceptable solution ( $\chi^2$ -minimum only about 15% higher than for the default roughness case), but the corresponding radiometric effective size was below 0.3 km, well outside the possible range. This confirms again that a certain roughness level is needed

---

<sup>6</sup> Active Cavity Radiometer Irradiance Monitor (ACRIM) total solar irradiance monitoring 1978 to present (Satellite observations of total solar irradiance); access date 2014-01-28; <http://www.acrim.com/>

to explain the available observations, even in case of highly detailed and structured shape models. In fact, the surface features in the Gaskell model still belong to the “global shape”. They are still large in comparison to the thermal skin depth scales<sup>7</sup>. Therefore it is needed to add an artificial roughness to account for the thermal beaming effect (Lagerros 1998b). This effect occurs mainly at centimetre scales, with small contributions coming from surface porosity on smaller scales (Hapke 1996; Lagerros 1998a). Multiple scattering of radiation increases the total amount of solar radiation absorbed by the surface and rough surface elements oriented towards the Sun become significantly hotter than a flat surface (Rozitis & Green 2011). Without such a “beaming model” on top of the Gaskell model it was not possible to find a convincing radiometric solution for all observations simultaneously. Here we used (as before for the spherical and Kaasalainen shape models) the beaming model concept developed by Lagerros (1997), with  $\rho$ , the r.m.s. of the surface slopes and  $f$ , the fraction of the surface covered by craters. The beaming model produces a non-isotropic heat radiation, which is noticeable at phase angles close to opposition (see also figure 8). But it also influences the shape of the SED in the mid-IR which is very relevant for our data set (e.g., Müller 2002). But more thermal data closer to opposition would be needed to fully characterise surface roughness properties of Itokawa.

### 3.4.3. Limitations of the TPM

We combined the Gaskell shape model (accepting the Gaskell size scale) now with our derived thermal properties: an intermediate roughness level ( $f=0.7$ ,  $\rho=0.6$ : 70% of the surface covered by craters with a surface slope r.m.s. of 0.6) and a thermal inertia of  $700 \text{ J m}^{-2} \text{ s}^{-0.5} \text{ K}^{-1}$ . In figure 5 we present the ratios between observed fluxes and the corresponding TPM predictions and show this ratios as a function of phase angle, wavelength, and rotational phase. These kind of plots are very sensitive to changes in the thermal properties (a full discussion of the influences is given in Müller 2002): a wrong thermal inertia would lead to slopes in the phase-angle picture (top in figure 5) with large deviations from 1.0 at the largest phase angles, while wrong beaming parameters are dominating at the smallest phase angles close to opposition. The wavelength picture (bottom in figure 5) gives indications about emissivity variations and is strongly reacting to beaming parameter variations, especially at wavelengths shorter than the peak wavelength. The observation/TPM ratios also change with different aspect angles and the different sets of measurements are not easy to compare. Our optimum TPM solution seems to combine the available observations without any obvious remaining trend in phase angle, wavelength or rotational phase.

Nevertheless, there are individual outliers where observations and model predictions differ significantly. Some of the data at phase angles above  $100^\circ$  (also visible in figure 5 middle

---

<sup>7</sup> The 49,152 facet shape model has an average facet dimension of  $\sim 4 \text{ m}$  whilst the highest resolution  $\sim 3$  million facet shape model has an average facet dimension of  $\sim 0.5 \text{ m}$ . Both of which are much larger than Itokawa’s implied thermal skin depth of about 1 cm.

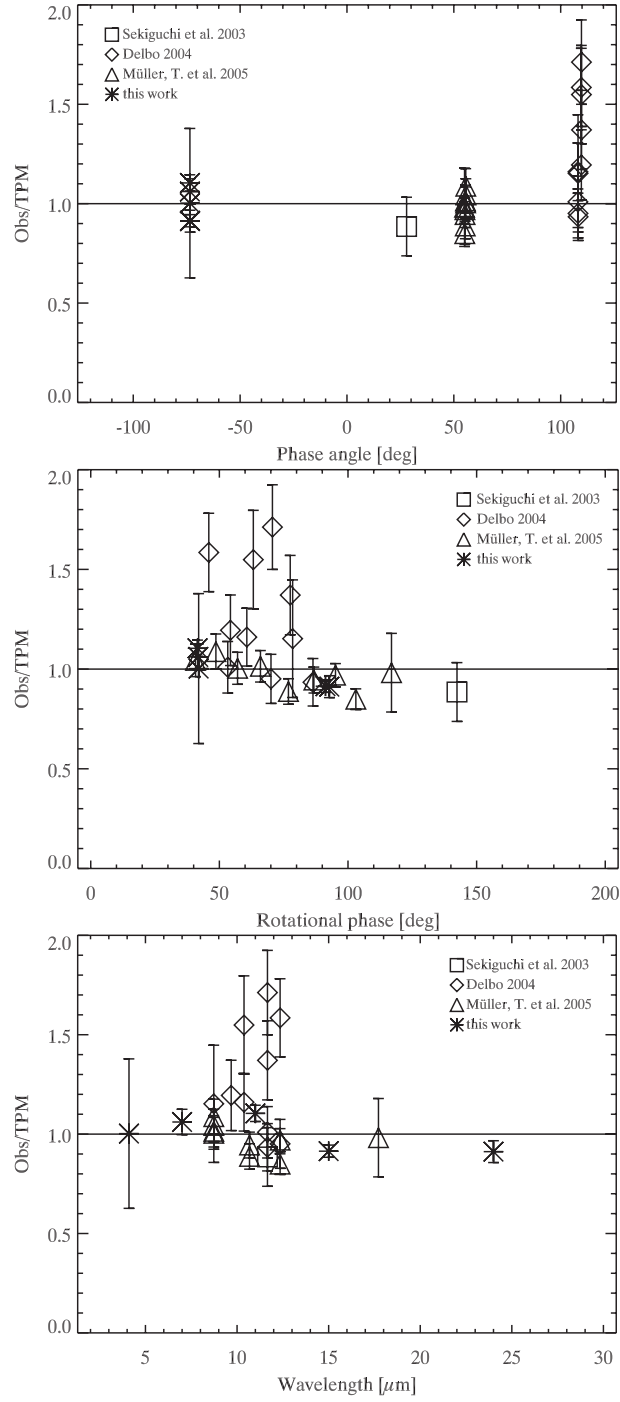


**Fig. 5.** All thermal observations divided by the corresponding TPM prediction as a function of phase angle (top), as a function of rotational phase (middle) and as a function of wavelength (bottom), with the zero rotational phase in the TPM setup defined at JD 2451934.40110 or 2001-Jan-24 21:37:35 UT).

and bottom) are very problematic in the TPM calculations. According to Delbó et al. (2004) the quality of some of the measurements is poor, but it could also well be that the TPM temperature calculations are not correct and that instead of a 1-D heat conduction a 3-D heat conduction would be required for some of the extreme viewing and illumination geometries (see also discussions by Davidsson et al. 2010). The 1-D heat conduction seems to work fine in case of simple shape models, but if a shape model has many small-scale features then the lateral heat conduction might influence the true surface temperatures considerably at least at very large phase angles. Another reason for the offset at large phase angles could be related to the approximate treatment of heat conduction inside the craters (see Section 3.1). Rozitis & Green (2011) showed that the rough surface thermal emission is enhanced slightly on the night side because of the mutual self-heating of the interfacing rough surface elements. This could be another explanation why our TPM predictions are lower than the observed fluxes at high phase angles in Fig. 5 (top).

The  $\chi^2$ -analysis using the Gaskell shape model is almost identical to the analysis using the Kaasalainen shape model: We obtained very similar  $\chi^2$ -values and also the derived thermal properties agree very well. This shows that our analysis is limited by the number and quality of the thermal observation and not by shape information. The uncertainties are pure r.m.s.-values from the 25 individually derived radiometric solutions, but they reflect to a certain extent also uncertainties in surface roughness and thermal inertia and the quality of the mid-IR photometric data points.

## 4. Model Comparison and Predictions

### 4.1. Thermal light-curve comparison

Now, with the true shape model at hand, it is interesting to compare thermal light-curves from the Kaasalainen shape model with the light-curves from the Gaskell shape model. In figure 6 we calculated for one full rotation period with a starting time 01-Jul-2004 at 00:00 UT the visual light-curve (in relative magnitudes), based on the Gaskell shape-model (top), and the thermal light-curves (bottom) at different wavelengths (8.73, 10.68, 12.35, 17.72  $\mu\text{m}$ ). At visible wavelength the Kaasalainen-shape model matches very well the existing light-curves (Kaasalainen et al. in press; Āurech et al. 2008). In the mid-IR thermal range the results of the Kaasalainen shape model follows for large fractions of the light-curve from the Gaskell model. But at specific rotational phases the differences are significant. The Kaasalainen shape model produces a larger peak-to-peak thermal light-curve amplitude, nicely visible in the Q-band at 17.72  $\mu\text{m}$  curve and it also produces bumps and sharp edges at certain phases.

The relatively large facets in the Kaasalainen shape model cause artificial structures in the predicted thermal light-curve while the Gaskell model produces astonishingly smooth and regular curves. In the given observing set there are also severe differences in the peak-to-peak



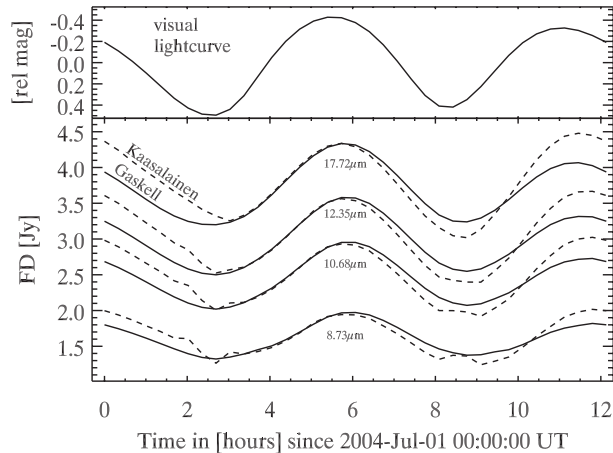


**Fig. 6. Top:** The visual light-curve in relative magnitudes, based on the Gaskell shape-model. **Bottom:** A comparison of thermal light-curves produced with the Kaasalainen shape model (dashed lines) and the Gaskell shape model (solid lines) for the epoch 01-Jul-2004 when the asteroid was seen at phase angles of  $54\text{--}55^\circ$ .

variations from both models (about 10-20%, depending on the wavelength), but the deviations vary not only with wavelength, but also with aspect angle. The minima in the thermal light-curve are also broader than for the visual light-curve. This is an effect of the object’s shape at a given rotation angle combined with the high thermal inertia which smoothes out the rapid changes of illuminated surface areas. It can be concluded that the Kaasalainen shape model, although it was derived from light-curve observations and matches nicely visual light-curves for a wide range of observing geometries, still has shortcomings in the context of thermal light-curves. Or in other words: the light-curve inversion technique might benefit from using thermal light-curves and the resulting shape models and spin-axis orientations would come closer to reality.

#### 4.2. TPM predictions using the Gaskell shape model

The Gaskell shape model in combination with the derived and validated thermophysical properties allows now to do more generalised studies. What can be learnt from thermal spectra or light-curve measurements at different wavelengths? How does the opposition effect look like at thermal wavelengths? What are the key observing geometries for successful radiometric calculations?

Figure 7 (top) shows model predictions (now only using the Gaskell shape model) for a wavelength range from 5 to  $50\ \mu\text{m}$ . Both SEDs at intermediate roughness level were normalised to 1.0 at the thermal emission peak wavelengths. Nevertheless, one can see that the SED at small phase angles (dashed lines) are higher (in the longer wavelength range) than the SEDs at larger phase angle (solid lines). The surface roughness and its thermal-infrared beaming effect enhance the observed thermal emission at low phase angles. This is then balanced out by a

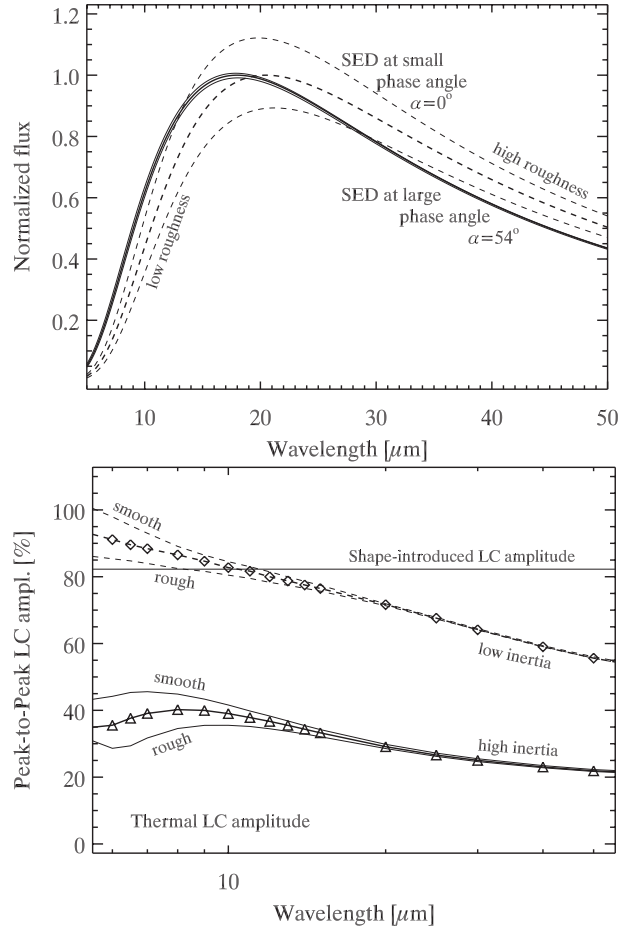


**Fig. 7.** The Gaskell shape model combined with thermal properties: Thermal effects as a function of wavelength. **Top:** The normalised SEDs for observations close to opposition (dashed lines) and at  $54^\circ$  phase angle (solid lines) for a thermal inertia of  $\Gamma=1000 \text{ J m}^{-2} \text{ s}^{-0.5} \text{ K}^{-1}$ . The strong roughness influence at small phase angles is clearly visible (thermal opposition effect). **Bottom:** The thermal light-curve (LC) amplitudes (peak-to-peak in [%] of the absolute thermal flux) for the observing constellation on 01/Jul/2004 ( $54^\circ$  phase angle). For the “low thermal inertia” case we used  $15 \text{ J m}^{-2} \text{ s}^{-0.5} \text{ K}^{-1}$  (typical value for large main-belt asteroids; Müller et al. 1999) and for the “high thermal inertia”  $1000 \text{ J m}^{-2} \text{ s}^{-0.5} \text{ K}^{-1}$ . The pure shape-caused light-curve amplitude (as seen in visual light) is indicated by the horizontal line. The peak-to-peak amplitude decreases significantly for longer wavelengths and for higher thermal inertias.

reduced thermal emission at larger phase angles to conserve energy (see also Müller 2002). The SEDs close to opposition (dashed lines) are strongly influenced by variations in the roughness, while at larger phase angles (solid lines) the roughness properties play only a minor role. The flux enhancements observed at low phase angle are dominated by limb surface enhancements. Some of the surface elements inside craters located near the terminator are orientated towards the Sun. The corresponding temperature enhancements are much greater than those achieved at the bottom of craters near the subsolar region. The resulting beaming effect is more efficient at low phase angles, where the observer is able to see the illuminated crater walls which produce additional thermal flux. This limb-brightening effect has been seen in spatially resolved measurements, and it has been successfully modelled for the Moon (Rozitis & Green 2011) and for (21) Lutetia (Keihm et al. 2012). The lack of small phase angle thermal observations explains our difficulties to find a robust solution for Itokawa’s surface roughness. Observations close to opposition would constrain these properties much better. Figure 7 (bottom) shows the behaviour of the thermal light-curve (at phase angle  $54^\circ$ ) as a function of wavelength for two values of the thermal inertia. The “low thermal inertia” case represents typical main-belt values (Müller et al. 1999) caused by a very well insulating dust regolith on the surface ( $15 \text{ J m}^{-2} \text{ s}^{-0.5} \text{ K}^{-1}$ ). For comparison, the Moon has a thermal inertia of  $39 \text{ J m}^{-2} \text{ s}^{-0.5} \text{ K}^{-1}$  (Keihm 1984). The “high thermal inertia” case corresponds to our best solution for the thermal properties of (25143) Itokawa. In the given geometry the peak-to-peak brightness variation during one full rotational period is changing dramatically with wavelength. At mid-IR the amplitude in the “low thermal inertia” case can even exceed the pure shape-caused brightness variation! The thermal light-curve amplitude decreases by more than a factor of 2 from mid-IR to far-IR wavelengths and this effect is almost independent of phase angle. In the high thermal inertia case (Itokawa) the overall values are significantly smaller (much smaller than the shape-introduced amplitude) and also the change with wavelength is smaller. Close to opposition the light-curve amplitude behaviour in the high thermal inertia case is more complex and does not show a clear trend with wavelength anymore. Overall, the peak-to-peak thermal light-curve amplitude decreases for higher thermal inertias and at longer wavelengths. Uncertainties in the light-curve amplitudes due to stronger influences of surface roughness increase for observations close to opposition.

In figure 8 we averaged the flux predictions over a complete rotation and looked at the changes with phase angle covering large periods before and after opposition. The predictions have been normalised at  $\alpha = 0^\circ$  and for default roughness. The flux change is dominated by the distance change between Earth and asteroid. The error bars indicate the uncertainties due to thermal inertia, the dashed lines give the boundaries for very low and high beaming values, i.e. low and high surface roughness. At small phase angles there is another effect visible: the thermal opposition or beaming effect. At small phase angles it is possible to see warmer temperatures inside the small-scale surface structures (modelled by the crater-like

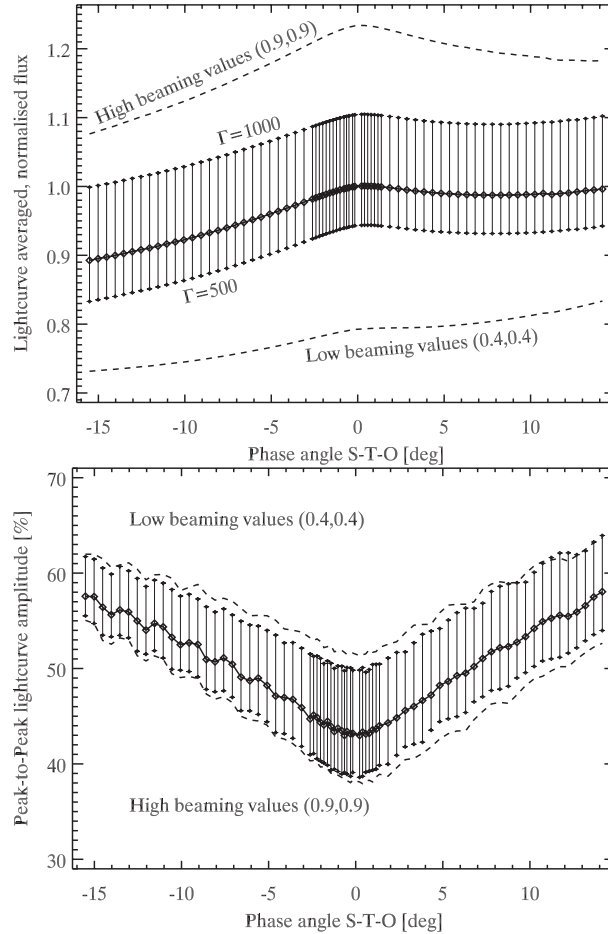


**Fig. 8.** TPM/Gaskell predictions for Itokawa-opposition in 2011. The corresponding times are: 03-Apr-2011:  $-15.0^\circ$  (trailing the Sun), 13-Jun-2011:  $0.1^\circ$ , 27-Aug-2011:  $+15.0^\circ$  (leading the Sun). **Top:** Normalised (by the asteroid distance to Sun and Earth)  $10\ \mu\text{m}$  fluxes as a function of phase angle. Uncertainties due to thermal inertia (range from  $500\text{-}1000\ \text{J m}^{-2}\ \text{s}^{-0.5}\ \text{K}^{-1}$ ) are given with error bars, uncertainties due to roughness (range for  $(\rho, f)$  from  $(0.4, 0.4)$  to  $(0.9, 0.9)$ ) are indicated by the dashed lines. The opposition “peak” at small phase angles can be seen, as well as the influence of surface roughness on the peak-height. **Bottom:** the peak-to-peak light-curve variation at  $10\ \mu\text{m}$  in percent as a function of phase angle. The relative light-curve amplitude is significantly smaller close to opposition. The influences of roughness and thermal inertia change slightly with phase angle.

TPM roughness implementation), mainly located near the terminator (see above). Overall, this leads to enhanced thermal fluxes at small phase angles which is not the case in simple thermal models with constant phase angle corrections or if the surface roughness is omitted. During both oppositions also the total peak-to-peak light-curve amplitude changes significantly with the smallest amplitudes close to opposition. These figures show that each data set puts different constraints on the thermal properties. Observations at small phase angles show the smallest thermal light-curve amplitudes (bottom of figure 8). Thermal light-curve measurements at large phase angles ( $> 30^\circ$ ) and close to the emission peak (in the mid-IR for NEAs) are providing the most stringent constraints on the thermal inertia: the light-curve amplitude is maximal and the beaming influence is very small.

We also looked into synthetic thermal light-curves for the Akari observing epochs and using the Gaskell shape model. Figure 9 shows these light-curves at  $4.1$  (top) and  $15.0 \mu\text{m}$  (bottom) for a wide range of thermal inertias. The TPM code produces absolute fluxes which compare very well with the derived Akari flux densities which are over-plotted in the figures. Our calculations show that the thermal light-curves change dramatically with changing thermal inertia. At  $4.1 \mu\text{m}$  the light curve shape goes from a relatively smooth curve with two different peak levels (low thermal inertia) to a much more structured curve with sharp turns (high thermal inertia). The amplitude is not very much affected, but the delay times of the curves increase with increasing thermal inertia. In the high thermal inertia case the thermal emission peaks happen much later and delay times of up to 2 hours are found. At these short wavelengths it is mainly the hottest sub-solar terrains which dominate the observed fluxes and flux changes. But due to the roughness-thermal inertia degeneracy (e.g. Rozitis & Green 2011) the short-wavelength observations are not ideal for deriving highly reliable size-albedo solutions. However, the shift of the thermal curves with respect to a purely shape-driven light-curve are closely connected to the object's thermal inertia. Monitoring light-curve changes over part of the rotation period is therefore the recommended approach at the short wavelengths. At  $15.0 \mu\text{m}$  the situation is different: the light-curves are in general much smoother and their shapes do not change much with thermal inertia, and the peak thermal emission delay times are smaller than at shorter wavelengths. These measurements usually lead to more robust size-albedo due to the reduced influence of the roughness-thermal inertia degeneracy (e.g. Müller 2002). Accessing the object's thermal inertia is more difficult: either one has to measure the thermal light-curve amplitude (which is substantially decreasing with increasing thermal inertia) or one has to combine the measurements with observations at different phase angles. It is also worth to note here that the thermal light-curve shapes, amplitudes, delay times for a given object also depend on the phase angle. The Akari measurements were taken at a phase angle of  $73^\circ$  where the illuminated (hot) part of the surface dominates the short wavelength observations, while at longer wavelengths there are also flux contributions from the warm, non-illuminated parts which have just rotated out of the Sun.

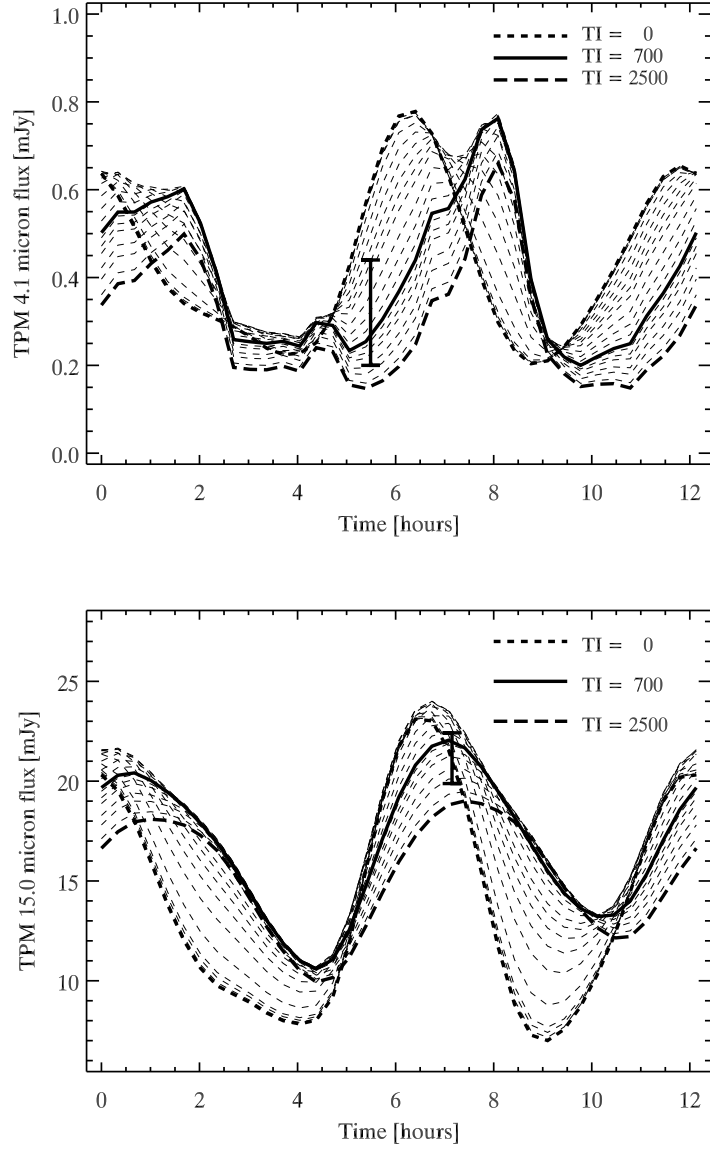


**Fig. 9.** TPM/Gaskell thermal light-curve predictions for Itokawa during the Akari observing epochs for a wide range of thermal inertias. **Top:** calculated thermal light-curves at  $4.1\ \mu\text{m}$  together with the observed Akari data point. **Bottom:** calculated thermal light-curves at  $15.0\ \mu\text{m}$  together with the observed Akari data point.

## 5. Discussion

### 5.1. TPM with spherical shape model

The interpretation of the 30 thermal infrared observations by using only a spherical shape model (Sect. 3.2) was very successful: the radiometric effective size prediction lies within a few percent of the true, in-situ value, the radiometric albedo prediction agrees within the error-bars with Bernardi et al. (2009), the retrograde sense of rotation was clearly favoured in the optimisation process, and thermal inertia values in the range  $500\text{-}1500 \text{ J m}^{-2} \text{ s}^{-0.5} \text{ K}^{-1}$  are the most likely ones.

But the calculations benefited from the proximity of the assumed spin axis orientation with the true orientation and from using a realistic rotation period. If an object’s rotation period is very different from the TPM assumptions and/or the spin vector is far away from the ecliptic pole direction the TPM predictions will be less reliable. Also the number of thermal observations, their distribution in phase angle space, in wavelength space, in rotational phase space, in aspect angle space and observing geometry influence the quality of the TPM outcome.

Overall, the reduced  $\chi^2$ -values are relatively high, indicating that the spherical shape is not always allowing to produce model predictions within the given observational errors. The model predictions for the few cases of extreme cross-sections dominate the overall  $\chi^2$ -sums. But here the observations are statistically distributed over rotational phases and aspect angles and the  $\chi^2$ -values remain sensitive to basic object properties like thermal inertia and sense of rotation. If only very few thermal observations would be available, even the distinction between pro- and retrograde solutions could fail for cases where shape effects and/or phase angle effects interfere with thermal signatures in the terminator region. Müller (2002) demonstrated the capabilities and limitations of the “radiometric method” to determine the sense of rotation via very spherical shape models. Based on a sample of 9 main-belt asteroids with comparable sets of thermal observations before and after opposition, the thermal data indicated the correct sense of rotation for 8 objects. In one case it failed, very likely due to shape and cross-section effects and data sets which did not cover the full rotation periods.

Nevertheless, our extremely simplified model approach shows the large potential of the radiometric technique: Assuming a spherical shape in combination with a realistic rotation period and a range of spin-axes it is possible to derive the sense of rotation and very accurate values for the effective size. But the key to robust results is the analysis of all thermal observations simultaneously, combined with all available information from visual photometry and light-curves observations. The very accurate radiometric diameter prediction has to be seen in comparison with the radar techniques: (Ostro et al. 2004; Ostro et al. 2005) used delay-Doppler images of (25143) Itokawa obtained at Arecibo and Goldstone to predict a size of  $594 \times 320 \times 288 \text{ m}$  ( $\pm 10\%$ ), i.e., an effective diameter of 379.7 m which is 16% higher than the Fujiwara et al. (2006) value of 327.5 m. In addition, the radar-technique can only be used

if the object has a close encounter with Earth, while thermal observations are much easier to obtain.

An important element of the thermal analysis is the reliability of the H- and G-values. Bernardi et al. (2009) published new values based on extensive light-curve data from phase angles close to opposition out to  $115^\circ$ . The new H-magnitude differs by 0.5 mag from the ones used in M05. This influences the albedo considerably (see discussion in M05) while the radiometric diameter is less affected. The difference in albedo ( $0.19_{-0.03}^{+0.11}$  in M05 and  $0.299 \pm 0.043$  from Sect. 3.4) is mainly caused by this 0.5 mag change in absolute magnitude.

Hasegawa et al. (2008), and later Müller et al. (2011), applied the TPM technique to thermal observations of the Hayabusa2 sample return target (162173) 1999 JU<sub>3</sub>. First, by using a spherical shape model, then by a modified shape model which would match the existing visual light-curves in amplitude and in phase. The quality of the resulting radiometric properties (diameter, albedo, thermal inertia, ...) suffered from an unknown spin vector orientation at the time of the calculations. Nevertheless, the example of (162173) 1999 JU<sub>3</sub> shows nicely the potential and the limitation of applying this method without knowing the precise shape nor the spin vector orientation.

## 5.2. TPM with Kaasalainen-/Radar-shape models

Using the shape model (together with the spin-vector orientation) from light-curve inversion techniques led to a radiometric diameter which was within 2% of the true in-situ result (M05; Fujiwara et al. 2006). The thermal observations put very strong constraints on the radiometric diameter. If, in addition, the H-G values are reliable, i.e., representing light-curve-averaged properties, or if simultaneous V-magnitudes are available, then both, the effective diameter and the albedo can be derived with high accuracy. Alternatively, the size information from radar techniques or occultation measurements can be tested with TPM calculations: Is it possible to find realistic thermal properties to explain thermal measurements and the independent size values simultaneously? M05 tried such an approach with Itokawa's radar size, but they could not find any acceptable match with the observed fluxes and they concluded that the radar size must be too large.

Our optimisation process clearly has limitations: Figure 4 demonstrates that the best solutions from using all 30 data points were strongly affected by a few less reliable observations. Thermal observations suffer in some cases from poor absolute calibration (or badly documented calibration), from high humidity weather conditions and/or high air-masses, or from uncertainties in the definition of band-passes with errors in the colour correction terms. The plots with observations/model ratios as a function of wavelength, phase angle and rotational phase revealed in many cases the outliers, at least if a high quality shape model (covering many aspect angles) is available.

Another limiting factor is the uncertainty in surface roughness. An artificial roughness



model is needed to explain typical mid-IR asteroid spectra (e.g., Barucci et al. 2002; Müller & Blommaert 2004; Dotto et al. 2000; Müller & Lagerros 2002), but the precise values or the interpretation of roughness is more complex: The thermal infrared observations are disk-integrated observations, averaging over very diverse surface regions. The resulting disk-integrated thermal properties, especially the roughness, are therefore of limited significance for characterising individual regions on the surface. Our “default” roughness model explains the existing observations very well, although it works in certain observing geometries better than in others, but more observations close to opposition (see figure 7) or at shorter wavelengths (e.g. Müller 2002 or Rozitis & Green 2011) would allow to narrow down the range in the possible roughness parameter space or to even to distinguish between hemispheres or large surface regions with different roughness properties. It should also be noted here that the roughness influences radiometric size and albedo solutions strongly if thermal infrared observations are only taken close to opposition and/or at short wavelengths in the Wien-part of the thermal emission.

Overall, the step from spherical to Kaasalainen shape model changed only slightly the effective diameter, geometric albedo and thermal inertia values, but the reliability improved significantly: The  $\chi^2$ -minima shrank from  $\sim 5$  to about 2.

### 5.3. TPM with Hayabusa/Gaskell-shape model

The availability of the full, high resolution shape model with spin-vector orientation and absolute size information (Demura et al. 2006) allows to obtain confidence in the radiometric technique: Using only the shape model and spin-vector orientation in combination with the set of thermal infrared observations we found the best fit to all data at a thermal inertia of  $700 \text{ J m}^{-2} \text{ s}^{-0.5} \text{ K}^{-1}$  and under the assumption of a “default roughness”. The corresponding radiometric effective diameter agrees then nicely with the true value. The radiometric diameter itself has a formal uncertainty of  $\pm 8\%$  when taking the r.m.s.-residuum from the 25 observations or  $8/\sqrt{25} = \pm 1.6\%$  when accepting that the observations represent 25 repeated measurements of the same property, i.e., the effective diameter of a equal volume sphere. The radiometrically derived albedo has a r.m.s.-value of  $\pm 15\%$  or a statistical error of the mean of about  $\pm 3\%$ . But in case of the albedo the dominating uncertainty is from the H-magnitude. The  $\pm 0.09/0.10$  mag error in H-value of 19.40 mag in combination with the true in-situ size value corresponds to a geometric albedo of  $0.29 \pm 0.03$ , i.e.,  $\pm 10\%$ . The influences of uncertainties in the thermal properties and the surface roughness only play a minor role in the final solutions which can be seen in figure 4 where the different curves have a very small scatter close to the optimum solutions. On the other hand, even the high resolution shape models require the addition of roughness on the surface to match the measured fluxes. These high resolution models include rocks, boulders, craters, valleys and mountains, i.e., the intermediate scales, but the centimetre scale is missing. The centrimetre-scale roughness plays an important role, because that is where the energy is reflected, absorbed, emitted, or conducted in the regolith. Images from the

Hayabusa mission with a spatial resolution of 70 cm per pixel (e.g., Saito et al. 2006) reveal very diverse surface morphology on intermediate scales (smooth, rough terrains) and very likely also on micrometre scale (solid boulders, smooth terrains, cratered rough terrains).

The radiometric technique can be considered as a very reliable (remote) technique for the determination of the effective size of small bodies. And the size information is needed not only for potentially hazardous objects, but also to investigate densities, size-frequency distributions, binary/multiple systems, formation process, etc. The technique only depends on the availability of thermal infrared observations and is not limited to close Earth encounters (like the radar-technique) or to only the very largest main-belt asteroids (like the adaptive optics technique).

The thermal inertia is an important parameter for small bodies in the Solar System, but only known for very few targets (e.g., Delbó et al. 2007). It is relevant when calculating the main non-gravitational orbit perturbations over time spans of centuries, caused by the Yarkovsky effect. It is a result of the way the asteroid's rotation affects the surface temperature distribution and therefore the anisotropic thermal re-emission (Vokrouhlický et al. 2000). The thermal inertia might also help to distinguish between solid rock surfaces which are expected to have very high thermal inertias well above  $1000 \text{ J m}^{-2} \text{ s}^{-0.5} \text{ K}^{-1}$  and regolith-covered bodies, like the Moon or large main-belt asteroids. (25143) Itokawa has an intermediate thermal inertia, possibly indicating a rubble pile structure where seismic waves reorganise the body's interior and the surface frequently and the formation of a thick regolith (with thermal inertias below  $100 \text{ J m}^{-2} \text{ s}^{-0.5} \text{ K}^{-1}$ ) is hampered. The reason for having very little fine regolith could also be related to the weak gravity on small, low density objects. Small asteroids tend to have in general higher thermal inertias (Delbó et al. 2007), but there are exceptions (e.g., Müller et al. 2004).

## 6. Conclusions

(25143) Itokawa is an extremely important test case for the validation process of thermophysical model techniques. The existing mid-IR observations allowed to evaluate the possibilities and limitations of different levels of complexity within our TPM implementation. Even in cases where very little is known about shape and spin behaviour it allows to derive reliable properties, like the effective size, the albedo and thermal properties without using any artificial model fudge factors. But the outcome is tightly connected to the availability and quality of thermal infrared observations. Ideally, the observations should (i) cover a sufficient wavelength range around the emission peak (several photometric bands or mid-IR spectra); (ii) include measurements before and after opposition; (iii) cover a large phase angle range, including measurements close to opposition; and, (iv) include a significant range of rotational phases and/or substantial parts of the thermal light-curve. It is also important to note here that some of the mid-IR bands might be affected by silicate emission (e.g. Emery et al. 2006), but the effect on

size-albedo solutions can only be estimated if full thermal spectra are available.

Our analysis showed that for (25143) Itokawa the interpretation of surface roughness properties is limited mainly due to the lack observations close to opposition. Nevertheless, Itokawa’s size, albedo and thermal inertia have been derived with unprecedented accuracy by only using remote, disk-integrated observations: a shape model from standard light-curve inversion technique and thermal infrared observations from ground and from AKARI. The optimum radiometric size agreed within 2% with the true value derived from Hayabusa measurements.

The TPM predictions using the true in-situ shape model showed: (i) that the shape models from light-curve inversion techniques produce artefacts in thermal light-curves and that low thermal inertia object (e.g., large main-belt asteroids) can have light-curve amplitudes exceeding the pure shape-introduced values; (ii) that the SEDs taken close to opposition are strongly influenced by properties of the surface roughness (figure 7, top) leading to a strong degeneracy between roughness and thermal inertia effects; (iii) that there exists a thermal opposition effect and how it looks like (figure 8, top), (iv) how the thermal light-curve amplitude changes with phase angle (figure 8, bottom); (v) that the thermal light-curve amplitudes decrease with wavelength and for higher thermal inertias (figure 7, bottom); (vi) that thermal light-curve delay times increase with thermal inertia and decrease for longer wavelengths (figure 9); (vii) that the thermal inertia and the sense of rotation play a big role when interpreting thermal infrared observations at large phase angles. (viii) that even the high resolution Gaskell shape model still require an additional small-scale roughness to explain the observed infrared fluxes.

Our findings are supported by TPM analysis of other spacecraft target asteroids. In this context one should mention some of the recent studies on (4) Vesta (Müller & Lagerros 1998; Müller & Lagerros 2002; Leyrat et al. 2012; Keihm et al. 2013), (21) Lutetia (Mueller et al. 2006; Lamy et al. 2010; O’Rourke et al. 2012; Keihm et al. 2012), (433) Eros (Mueller 2007), and (2867) Steins (Lamy et al. 2008; Groussin et al. 2011; Leyrat et al. 2011). In all these cases the radiometrically derived properties are remarkably consistent with the spacecraft investigations documented by Russell et al. (2012) for (4) Vesta, by Sierks et al. (2011) for (21) Lutetia, by Thomas et al. (2002) for (433) Eros, and by Keller et al. (2010) for (2867) Steins. The TPM radiometric technique is very powerful in deriving highly reliable absolute sizes, albedos, and thermal inertias from remote disk-integrated thermal measurements. But each of the available data points has to be considered in its true illumination and observing geometry. In this way it is also possible to extract information on the object’s spin properties as well as on its shape, especially for objects where standard lightcurve inversion techniques have difficulties to determine these parameters.

The validated model techniques can easily be used for other targets, including near-Earth and main-belt asteroids, trans-Neptunian objects or inactive cometary nuclei. The plots and figures can also be used to optimize observing strategies to exploit the full TPM capabilities. The key ingredient for the full exploitation of thermophysical model techniques and for the

determination of reliable object properties is the availability of well-selected and well-calibrated thermal infrared observations covering many aspect angles.

S. Hasegawa was supported by Space Plasma Laboratory, ISAS, JAXA. We would like to thank Johan Lagerros for very useful discussions and Robert Gaskell for providing the necessary documentation for the implementation of Itokawa's shape model.

## References

- Abe, M., et al. 2006a, *Science*, 312, 1334
- Abe, S., et al. 2006b, *Science*, 312, 1344
- Barucci, M. A., et al. 2002, *Icarus*, 156, 202
- Bernardi, F., Micheli, M., & Tholen, D. J. 2009, *Meteorit. Planet. Sci.*, 44, 1849
- Binzel, R. P., et al. 2001, *Meteorit. Planet. Sci. (Suppl.)*, 36, A20
- Bowell, E., Hapke, B., Domingue, D., Lumme, K., Peltoniemi, J., & Harris, A. W. 1989, in *Asteroids II*, ed. R. P. Binzel, T. Gehrels, & M. Shapely (Tucson: University of Arizona Press), 524
- Davidsson, B., Gutierrez, P. J., Rickman, H., & Warell, J. 2010, in *DPS 42nd Annual Meeting, BAAS*, 1401
- Delbó, M. 2004, PhD thesis, Freie Universität Berlin
- Delbó, M., Dell'Oro, A., Harris, A. W., Mottola, S., & Mueller, M. 2007, *Icarus*, 190, 236
- Demura, H., et al. 2006, *Science*, 312, 1347
- Dotto, E., et al. 2000, *A&A*, 358, 1133
- Đurech, J., et al. 2008, *A&A*, 488, 345
- Emery, J. P., Cruikshank, D. P., & van Cleve, J. 2006, *Icarus* 182, 496
- Fujiwara, A., et al. 2006, *Science*, 312, 1330
- Gaskell, R., et al. 2008, Gaskell Itokawa Shape Model V1.0. HAY-A-AMICA-5-ITOKAWASHAPE-V1.0, NASA Planetary Data System, 2008
- Groussin, O., Lamy, P., Fornasier, S., & Jorda, L. 2011, *A&A*, 529, A73
- Gundlach, B., & Blum, J. 2013, *Icarus*, 223, 479
- Hapke, B. 1996, *JGR*, 101, 16833
- Hasegawa, S., et al. 2008, *PASJ*, 60, 399
- Hasegawa, S., Müller, T. G., Kuroda, D., Takita, S., & Usui, F. 2013, *PASJ*, 65, 34
- Harris, A. W., & Lagerros, J. S. V. 2002, *Asteroids III*, ed. W. F. Bottke Jr. et al. (Tucson: University of Arizona Press), 205
- Ishiguro, M., et al. 2003, *PASJ*, 55, 691
- Kaasalainen, M., et al. 2003, *A&A*, 405, L29
- Kaasalainen, M., et al. , in *International Science Symposium on Sample Returns from Solar System Minor Bodies ~ The 1st HAYABUSA Symposium*, ed. H. Yano, A. Fujiwara, D. Yeomans, & M. Zolensky, (ASP Conference series), in press
- Keihm, S. J. 1984, *Icarus*, 60, 568

- Keihm, S. J., Tosi, F., Kamp, L., Capaccioni, F., Gulkis, S., Grassi, D., Hofstadter, M., Filacchione, G., Lee, S., Giuppi, S., Janssen, M., & Capria, M. 2012, *Icarus*, 221, 395
- Keihm, S. J., et al. 2013, *Icarus*, 226, 1086
- Keller, H. U., et al. 2010, *Science*, 327, 190
- Kitazato, K., et al. 2008, *Icarus*, 194, 137
- Lagerros, J. S. V. 1996, *A&A*, 310, 1011
- Lagerros, J. S. V. 1997, *A&A*, 325, 1226
- Lagerros, J. S. V. 1998a, *A&A*, 332, 1123
- Lagerros, J. S. V. 1998b, PhD thesis, Uppsala University
- Lamy, P. L., et al. 2008, *A&A*, 487, 1187
- Lamy, P. L., Groussin, O., Fornasier, S., Jorda, L., Kaasalainen, M., & Barucci, M. A. 2010, *A&A*, 516, A74
- Lebofsky, L. A., et al. 1986, *Icarus* 68, 239
- Leyrat, C., et al. 2011, *A&A*, 531, A168
- Leyrat, C., Barucci, A., Mueller, T., O'Rourke, L., Valtchanov, I., & Fornasier, S. 2012, *A&A*, 539, A154
- Lowry, S. C., Weissman, P. R., Hicks, M. D., Whiteley, R. J., & Larson, S. 2005, *Icarus* 176, 408
- Lowry, S. C., et al. 2014, *A&A*, 562, A48
- Mueller, M., Harris, A. W., Bus, S. J., Hora, J. L., Kassis, M., & Adams, J. D. 2006, *A&A*, 447, 1153
- Mueller, M. 2007, PhD thesis, Freie Universität Berlin
- Mueller, M., Delbo, M., Kaasalainen, M., Martino, M. D., Bus, S. J., & Harris, A. W., , in International Science Symposium on Sample Returns from Solar System Minor Bodies ~ The 1st HAYABUSA Symposium, ed. H. Yano, A. Fujiwara, D. Yeomans, & M. Zolensky, (ASP Conference series), in press
- Müller, T. G., & Lagerros, J. S. V. 1998, *A&A*, 338, 340
- Müller, T. G., Lagerros, J. S. V., Burgdorf, M., Lim, T., Morris, P. W., Salama, A., Schulz, B., & Vandenbussche, B. 1999, in: *The Universe as Seen by ISO*, ed. ed. P. Cox & M. F. Kessler (ESA-SP 427), 141
- Müller, T. G., & Lagerros, J. S. V. 2002, *A&A*, 381, 324
- Müller, T. G. 2002, *Meteorit. Planet. Sci.*, 37, 1919
- Müller, T. G., & Blommaert, J. A. D. L. 2004, *A&A*, 418, 347
- Müller, T. G., Sterzik, M. F., Schütz, O., Pravec, P., & Siebenmorgen, R. 2004, *A&A*, 424, 1075
- Müller, T. G., Sekiguchi, T., Kaasalainen M., Abe M., & Hasegawa S. 2005, *A&A*, 443, 347 (M05)
- Müller, T. G., et al. 2011, *A&A*, 525, 145
- Müller, T. G., et al. 2012, *A&A*, 548, 36
- Müller, T. G., et al. 2013, *A&A*, 558, 97
- Murakami, H., et al. 2007, *PASJ*, 59, 369
- Noguchi, T., et al. 2010, *Icarus*, 206, 319
- Ohba, Y., Abe, M., Hasegawa, S., Ishiguro, M., Kwiatkowski, T., Colas, F., Dermawan, B., & Fujiwara, A. 2003, *Earth Planets Space*, 55, 341
- O'Rourke, L., et al. 2012, *Planet. Space Sci.*, 66, 192

- Okada, T., et al. 2006, *Science*, 312, 1338
- Onaka, T., et al. 2007, *PASJ*, 59, 401
- Ostro, S. J., Benner, L. M., Nolan, M. C., Giorgini, J. D., Jurgens, R. F., Rose, R., & Yeomans, D. K. 2001, American Astronomical Society, DPS meeting 33, 41.13
- Ostro, S. J., et al. 2004, *Meteorit. Planet. Sci.*, 39, 407
- Ostro, S. J., et al. 2005, *Meteorit. Planet. Sci.*, 40, 1563
- Rozitis, B., & Green, S. F. 2011, *MNRAS*, 415, 2042
- Russell, C. T., et al. 2012, *Science*, 336, 684
- Saito, J., et al. 2006, *Science*, 312, 1341
- Sekiguchi, T., Abe, M., Bönhardt, H., Dermawan, B., Hainaut, O. R., & Hasegawa, S. 2003, *A&A*, 397, 325
- Sierks, H., et al. 2011, *Science*, 334, 487
- Spencer, J. R., Lebofsky, L. A., & Sykes, M. V. 1989, *Icarus*, 78, 337
- Thomas, P.C., et al. 2002, *Icarus*, 155, 18
- Thomas-Osip, J. E., Lederer, S. M., Osip, D. J., Vilas, F., Domingue, D., Jarvis, K., & Leeds, S. L. 2008, *Earth Planets Space*, 60, 39
- Usui, F., et al. 2011, *PASJ*, 63, 1117
- Vokrouhlický, D., Milani, A., & Chesley, S. R. 2000, *Icarus*, 148, 118
- Yano, H., et al. 2006, *Science*, 312, 1350